

This work was written as part of one of the author's official duties as an Employee of the United States Government and is therefore a work of the United States Government. In accordance with 17 U.S.C. 105, no copyright protection is available for such works under U.S. Law.

Public Domain Mark 1.0

<https://creativecommons.org/publicdomain/mark/1.0/>

Access to this work was provided by the University of Maryland, Baltimore County (UMBC) ScholarWorks@UMBC digital repository on the Maryland Shared Open Access (MD-SOAR) platform.

Please provide feedback

Please support the ScholarWorks@UMBC repository by emailing scholarworks-group@umbc.edu and telling us what having access to this work means to you and why it's important to you. Thank you.

PROCEEDINGS OF SPIE

SPIDigitalLibrary.org/conference-proceedings-of-spie

Ground calibration of the x-ray mirror assembly for the X-Ray Imaging and Spectroscopy Mission (XRISM) I-measurement setup and effective area

Rozenn Boissay-Malaquin, Takayuki Hayashi, Keisuke Tamura, Takashi Okajima, Toshiki Sato, et al.

Rozenn Boissay-Malaquin, Takayuki Hayashi, Keisuke Tamura, Takashi Okajima, Toshiki Sato, Lawrence Olsen, Richard Koenecke, Wilson Lara, Leor Bleier, Megan E. Eckart, Maurice Leutenegger, Tahir Yaqoob, Meng Chiao, "Ground calibration of the x-ray mirror assembly for the X-Ray Imaging and Spectroscopy Mission (XRISM) I-measurement setup and effective area," Proc. SPIE 12181, Space Telescopes and Instrumentation 2022: Ultraviolet to Gamma Ray, 121811U (31 August 2022); doi: 10.1117/12.2627563

SPIE.

Event: SPIE Astronomical Telescopes + Instrumentation, 2022, Montréal, Québec, Canada

Ground Calibration of the X-ray Mirror Assembly for the X-Ray Imaging and Spectroscopy Mission (XRISM)

I – Measurement Setup and Effective Area

Rozenn Boissay-Malaquin^{a,b,c}, Takayuki Hayashi^{a,b,c}, Keisuke Tamura^{a,b,c}, Takashi Okajima^b, Toshiki Sato^d, Lawrence Olsen^e, Richard Koenecke^{e,f}, Wilson Lara^{e,g}, Leor Bleier^h, Megan E. Eckartⁱ, Maurice Leutenegger^b, Tahir Yaqoob^{a,b,c}, and Meng Chiao^j

^aCenter for Space Science and Technology, University of Maryland, Baltimore County (UMBC), Baltimore, Maryland, USA

^bX-ray Astrophysics Laboratory, NASA / Goddard Space Flight Center (GSFC), Greenbelt, Maryland, USA

^cCenter for Research and Exploration in Space Science and Technology, NASA / GSFC (CRESST II), Greenbelt, Maryland, USA

^dDepartment of Physics, Rikkyo University, Tokyo, Japan

^eInstrument Development Group, NASA / Goddard Space Flight Center (GSFC), Greenbelt, Maryland, USA

^fAdnet Systems Inc., Bethesda, Maryland, USA

^gBGE Technology LLC, Rockville, Maryland, USA

^hFlight Software Systems Branch, NASA / Goddard Space Flight Center (GSFC), Greenbelt, Maryland, USA

ⁱLawrence Livermore National Laboratory, Livermore, California, USA

^jInstrument/payload systems engineering branch, NASA / Goddard Space Flight Center (GSFC), Greenbelt, Maryland, USA

ABSTRACT

We present a summary of the ground calibration of the X-ray Mirror Assemblies (XMAs) for the XRISM satellite, that has been performed at the X-ray beamline at NASA's Goddard Space Flight Center. We used a scan method with a narrow X-ray pencil beam to calibrate both Resolve and Xtend XMAs, at eight different energies. In this paper, we give an overview of the measurement setup, and show the resulting on-axis and off-axis effective area response. Results of imaging performance, stray light, and performance variation across the aperture will be presented in separate publications.

Keywords: X-Ray Imaging and Spectroscopy Mission (XRISM), X-ray Mirror Assembly (XMA), X-ray Astronomy, Soft X-ray Telescope, Raster scan, Calibration, Optical performance, X-ray beamline

1. INTRODUCTION

The X-Ray Imaging and Spectroscopy Mission (XRISM, formerly XARM^{1–4}) is a mission developed under an international collaboration of Japan Aerospace Exploration Agency (JAXA), National Aeronautics and Space Administration (NASA), and European Space Agency (ESA), scheduled to be launched in early 2023. It will observe the Universe in X-rays with unprecedented sensitivity and spectral resolution, using its high-spectral-resolution imaging microcalorimeter and its large-field CCD imager, named Resolve and Xtend, respectively. Two X-ray Mirror Assemblies (XMAs⁵), that are conically approximated Wolter-I optics, have been developed for these instruments at NASA's Goddard Space Flight Center (GSFC) and completed in 2021. As XRISM is

Send correspondence to Rozenn Boissay-Malaquin: rozenbm@umbc.edu, or r.boissay@nasa.gov

Hitomi's (formerly ASTRO-H⁶) recovery mission, having similar scientific objectives,⁷ its mirror assemblies are designed identically to the soft X-ray telescopes (SXT^{8–12}) onboard Hitomi. Each XMA consists of 203 nested shells of thin foil reflectors, grouped in four quadrants with the support of radial bars, installed in primary and secondary housings. A pre-collimator, composed of nested cylindrical blades located above each reflector of the primary mirror, is used to minimize stray light events.¹³ The only major difference between SXTs and XMAs is the presence of an additional “dummy” primary foil and pre-collimator blade in XMAs, aiming to reduce stray light from the inner part of the telescope. The thermal environment of the XMAs is stabilized using a thermal shield¹⁴ placed above the pre-collimator, and heaters located on the perimeter of the XMA's housing. Each XMA weighs 42.5 kg, has a diameter of 45 cm, and has a nominal focal length of 5.6 m. Figure 1 shows a picture of both XMA flight models, developed at NASA/GSFC, without the thermal shields.



Figure 1. Picture of the XRISM X-ray Mirror Assemblies, without thermal shields (right: Resolve-XMA, left: Xtend-XMA).

The top-level performance requirements of the XMAs are an effective area of $>460 \text{ cm}^2$ at 1.5 keV and $>390 \text{ cm}^2$ at 6.4 keV, and an angular resolution of <1.7 arcmin. The measurement campaign of these XMAs at the 100 m X-ray beamline at NASA/GSFC aims to verify these requirements as well as a set of detailed calibration requirements. In this paper, we first present the measurement setup, describing the whole structure of the 100 m X-ray beamline at NASA/GSFC, the X-ray source, the monochromators and filters, the measurement chamber, the detectors (in Sec. 2.1), and the measurement methods (in Sec. 2.2). We briefly describe the ground calibration timeline in Sec. 3. We then report on the optical axis distribution of the quadrants (in Sec. 4.1), and on the on-axis and off-axis effective area response resulting from the ground calibration of both XMAs (in Sec. 4.2 and 4.3). Other measurements and results (imaging performance, stray light measurements, performance verification across the aperture) will be presented in separate publications.^{15,16}

2. MEASUREMENT SETUP

2.1 Beamline facility

We performed the calibration measurements of both XMAs at the 100 m X-ray beamline located at NASA/GSFC. A schematic top view of this facility is shown in Fig. 2. An X-ray source is located at one end of the system, while the measurement chamber is located at the other end. The Rigaku ultraX 18 X-ray generator used at this facility has a rotary anode target and provides high intensity X-rays, being able to reach a maximum of 60 kV and 300 mA. Different targets (C, Al, Ti, Fe, Cu, Mo, Ag, W, Pt) can be used to obtain a beam at the desired energy. X-rays are emitted when the electrons coming from the cathode filament collide with the anode target. Filaments of different sizes (0.1 x 1, 0.3 x 3, and 0.5 x 10 mm) can be used to control the X-ray spot size on the anode, which is of order 0.3 x 0.8 mm for the 0.3 x 3 mm filament. A bias voltage can be applied to focus the electrons,¹⁷ but we do not routinely use this option. By using different filaments, we performed our measurements with an X-ray spot size of 0.6 arcsec for the Al, Ti, Fe and Cu targets, and 1 arcsec for the Pt, Mo and Ag targets. This X-ray spot size could in theory affect the measurements and the beam divergence, but as we used a 15 x 15 mm beam to calibrate our >1 arcmin angular resolution XMA, the X-ray spot size is not a dominant source of beam divergence (see Sec. 2.2).

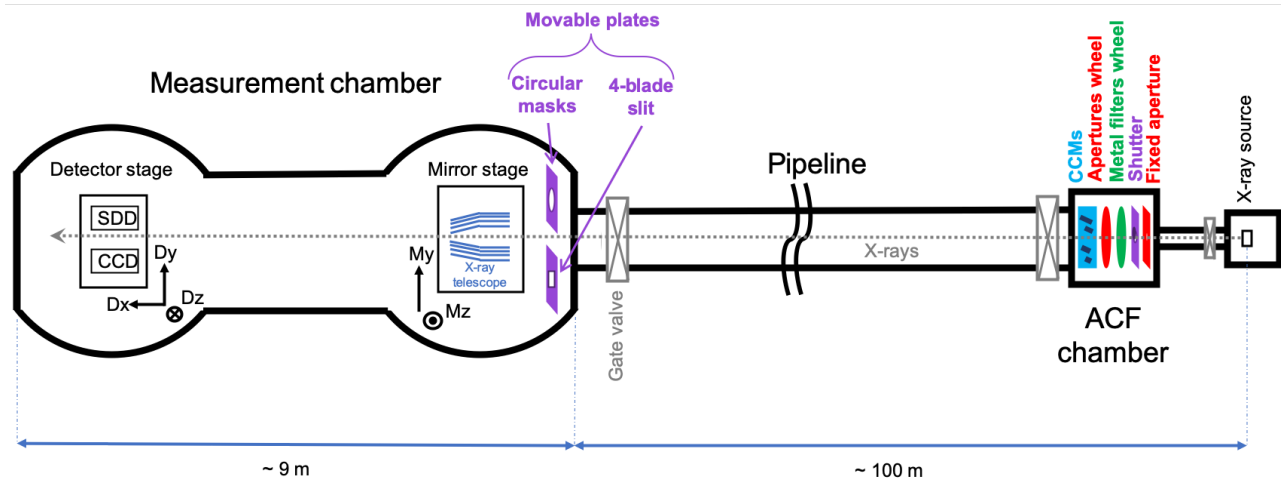


Figure 2. Schematic view of the beamline (top view).

A 9m-long measurement chamber is located at the other end of the 100m-long pipeline. This chamber contains the sample to be measured (the X-ray telescope), as well as detectors placed at its focal plane. Measurements can be performed either with a charge-coupled device (CCD) or a silicon drift detector (SDD). The TELEDYNE MTE-3 back-illuminated CCD has 2048 x 2048 pixels of 15 μm each. It is protected by a filter blocking infrared and optical contaminating light. The AMPTEK FAST SDD, with its effective surface of about 50 mm², can be used for a beam with a rate of up to 1,000,000 counts per second.

Both detector and mirror stages are movable, horizontally (in the Y direction, see Fig. 2) and vertically (in the Z direction). The distance between the telescope and the detectors can also be changed by moving the detector stage in the direction of the X-ray beam (along the X axis). The mirror stage can move around the X axis (θ_x), the Y axis (θ_y is the pitch angle) and the Z axis (θ_z is the yaw angle). The detector stage can be tilted around the X axis for adjustment. These movable stages allow us to perform X-ray telescope calibration, by using for example raster scans (see Sec. 2.2), and on and off-axis measurements (see Sec. 4).

The beam produced by the X-ray generator can be collimated by a 4-blade slit located right before the sample to be measured, inside the measurement chamber. Circular masks can be used instead, for example to illuminate only one quadrant of the telescope at a time. Both of these items are located on movable plates that can be placed, if necessary, right upstream from the telescope.

Different metal filters (Al, Mn, Ni, Zr, Nb, Pd) of several thicknesses can also be placed in the beam, via filter wheels located in the ACF (Aperture-Crystal-Filter) chamber downstream from the X-ray source (see Fig. 2). The beam size can also be adjusted using apertures of variable diameters, thanks to an aperture wheel located in this same chamber. Channel-cut crystal monochromators (CCMs) can also be moved in the path of the beam to obtain monochromatic X-rays. Two different crystals are available in the ACF chamber: the Si (111) crystal is used to get energies in the 2-7 keV range, while the Si (220) crystal is used for energies between 7 and 25 keV. An X-ray shutter is also located in the ACF chamber.

All the stages, filters, crystals, plates, source and detectors are controlled with a custom-built software, utilizing Python on the backend and a Qt-based GUI, which is designed to allow us to perform single and/or complex sequential measurements.

The whole apparatus is under vacuum, and its different parts (measurement chamber, pipeline, ACF chamber, and X-ray source) can be isolated from each other using several gate valves. By using two turbo pumps, the measurement chamber can be pumped down to a pressure of 10⁻⁵ Torr (required for our calibration measurements) in about 5 hours, and it can achieve a pressure of low 10⁻⁶ Torr in a few days.

2.2 Measurement methods

X-rays emitted by celestial objects are almost parallel when they reach our telescopes. Such a configuration is extremely difficult to reproduce in a lab. We first use a large-size diverging beam to fully illuminate the telescope, with a small X-ray source located at a much larger distance than the focal length of the telescope (about 100 m versus a focal length of 5.6 m). It is then necessary to correct the position of the detectors used for the calibration measurements, as the focal length becomes a bit larger due to the lens effect.

The problem when using diverging beam is that the tight nesting of the reflectors constituting the XMA prevents the illumination of a portion of the primary reflectors, because of the shadowing by the inner reflectors, and part of the X-rays reflected by the primary mirror does not reach the secondary mirror, because of the incident angle of the diverging beam. In this case, X-rays irradiate only 55% of the foil area, so we need some assumptions and models to evaluate the imaging performances and effective area.¹⁸

The 100m-long beamline at NASA/GSFC has recently been upgraded to allow measurements with a pencil beam with a small diverging angle, allowing the illumination of the entire aperture of the telescope via raster scan.^{19–22} The small diverging angle of the pencil beam renders vignetting negligible, allowing an accurate measurement of effective area and imaging performance. For the calibration of XMA, we thus use an X-ray pencil beam collimated to 15 x 15 mm (30 arcsec divergence) by a slit located right upstream from the telescope (see Fig. 2). The mirror and detector stages move synchronously, scanning the entire aperture of the telescope, following a path as shown for example in Fig. 3. To correct the divergence, the distance between the detector and the mirror is 1.06 times the nominal focal length, and the detector moves 1.06 times faster than the mirror. The fluctuation of the stage movement during the raster scan affects particularly PSF measurements for mirrors with a high angular resolution, so in this case the use of a diverging beam is preferable.²³ But for our arcmin level mirrors, this fluctuation is not a concern, so we used the raster scan with a pencil beam for direct measurements.

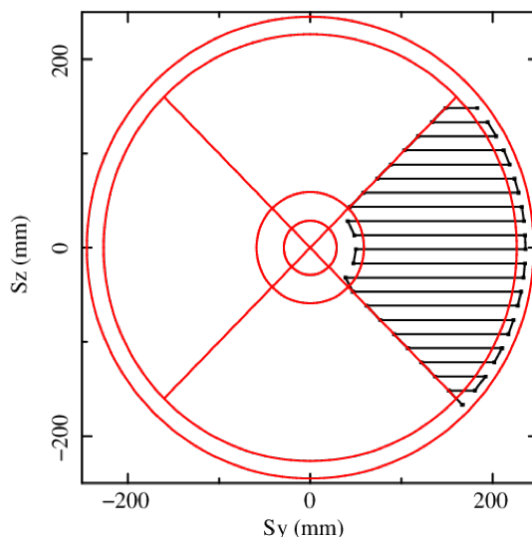


Figure 3. Example of raster scan path, for one single quadrant, with a 15 mm vertical pitch.

3. GROUND CALIBRATION TIMELINE

In order to analyze scientific observation data, we need to know the effective area of the XMA, which depends on the energy and on the off-axis and roll angles of the incident photons. We performed accurate measurements of effective area and image quality from August 2021 to March 2022 for Resolve-XMA, and from March 2022 to May 2022 for Xtend-XMA. Using the raster scan method (see Sec. 2.2), we scanned the entire telescope aperture with a 15 x 15 mm pencil beam, at different angles, and at eight different energies between 1.5 keV and 22.2 keV, using Al, Ti, Fe, Cu, Pt, Mo, and Ag targets, for both XMA.

The measurement plan for each XMA is described below:

- Alignment and search for optical axis
- On and off-axis responses at 6.4 keV
- Spot scan images
- On and off-axis responses at 9.4 and 11.1 keV
- On and off-axis responses at 8 keV
- Continuum on-axis scan with the Cu target
- On and off-axis responses at 4.5 keV
- On and off-axis responses at 17.5 keV
- Stray light measurements
- Local vignetting curve scan
- On-axis measurement at 22.2 keV (Resolve only)

The effective area function is the result of the performance of small parts of the XMA's aperture. For this reason, we took about 1600 snapshots by spotting a small area of 10 x 10 mm using a 6.4 keV beam across the XMA aperture. These spot scan images provide information about variations of the effective area, image profile and focal length. We also performed a local vignetting curve scan, aiming to measure the optical axes of each of the small areas described above. All these measurements, together with in-flight calibration measurements,²⁴ will be used in particular to update calibration files and software algorithms.²⁵ We present in Sec. 4 the results of the optical axis determination, and the on and off-axis effective area at different energies. Imaging performance and stray light measurements will be presented in a separate publication.¹⁵ Performance variation across the aperture, measured with spot scans, will be presented in detail in another presentation.¹⁶

4. EFFECTIVE AREA

The effective area (EA) $S_{\text{eff}}(E)$ is calculated using the following formula:

$$S_{\text{eff}}(E) = \frac{v_y h_z C_{\text{scan}}}{I}, \quad (1)$$

where v_y is the scanning speed in the horizontal direction, h_z is the scanning pitch in the vertical direction, I is the photon count rate of the incident beam, and C_{scan} is the number of collected photons (in a circle with a radius of 8') from all the raster scan paths. For our calibration measurements, we typically used $v_y = 4\text{mm/s}$ and $h_z = 15\text{mm}$, with a beam size of 15 x 15 mm.

4.1 Optical axis distribution

We first determined the optical axis of the whole telescope for both XMAs, by measuring the effective area at several off-axis angles in both yaw and pitch directions (-8', -4', 0', +4' and +8'), using the Fe K α line at 6.4 keV and the raster scan method. The optical axis was thus found at the peak of the effective area by fitting these vignetting curves with a Lorentzian model. We then aligned both XMAs to their respective whole-telescope optical axes.

To determine the optical axis of each quadrant, we then performed vignetting measurements for each quadrant at 6.4 keV, at different off-axis angles (0.5', 1', 1.8', 3', 4.5', 6' and 9' for Resolve-XMA, and 1.8', 5', 10', 15' and 20' for Xtend-XMA), in 4 directions (i.e. 8 roll angles, or azimuthal angles), as shown for example on the left of Fig. 4. On the right of Fig. 4, we show the example of the effective area map obtained by the measurements performed on Q1 of Resolve-XMA. In order to determine accurately the quadrant optical axes, we applied a 2D fitting to these vignetting data, with the sum of Gaussian and Lorentzian models, using the *lmfit* least-square fitting method in Python. The resulting quadrant optical axes for both XMAs are shown in Fig. 5. The distribution of the quadrants' optical axes is quite large, in a range of about 1.5 arcmin. The distribution of Resolve-XMA quadrants is slightly narrower than in Xtend-XMA.

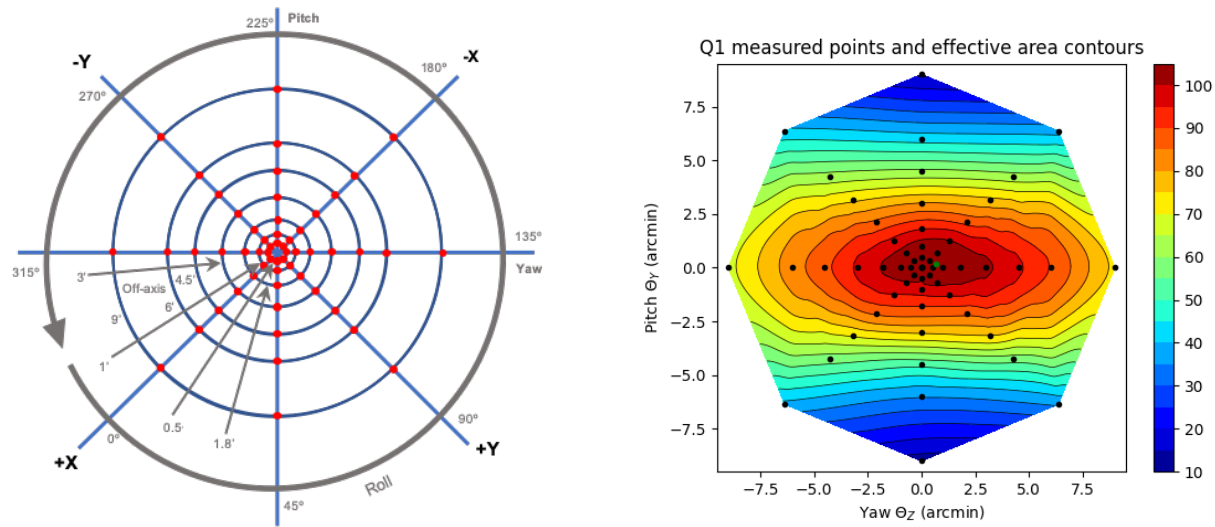


Figure 4. Example of off-axis points measured for vignetting curves; On the left, scheme of measurements points (red points) with the iron target, at 6.4 keV, at 7 off-axis angles (blue circles) and 8 roll angles (blue radial lines), for Resolve-XMA. The X and Y directions on this figure are different from the axes of the beamline, they represent the coordinates of the telescope (Q1 is in between +X and +Y, Q2 between +Y and -X, Q3 between -X and -Y, and Q4 between -Y and +X); On the right, effective area color map of Q1 of Resolve-XMA, measured at the corresponding angles (black points), used to determine the quadrant optical axis (represented by the green point) via 2D fitting.

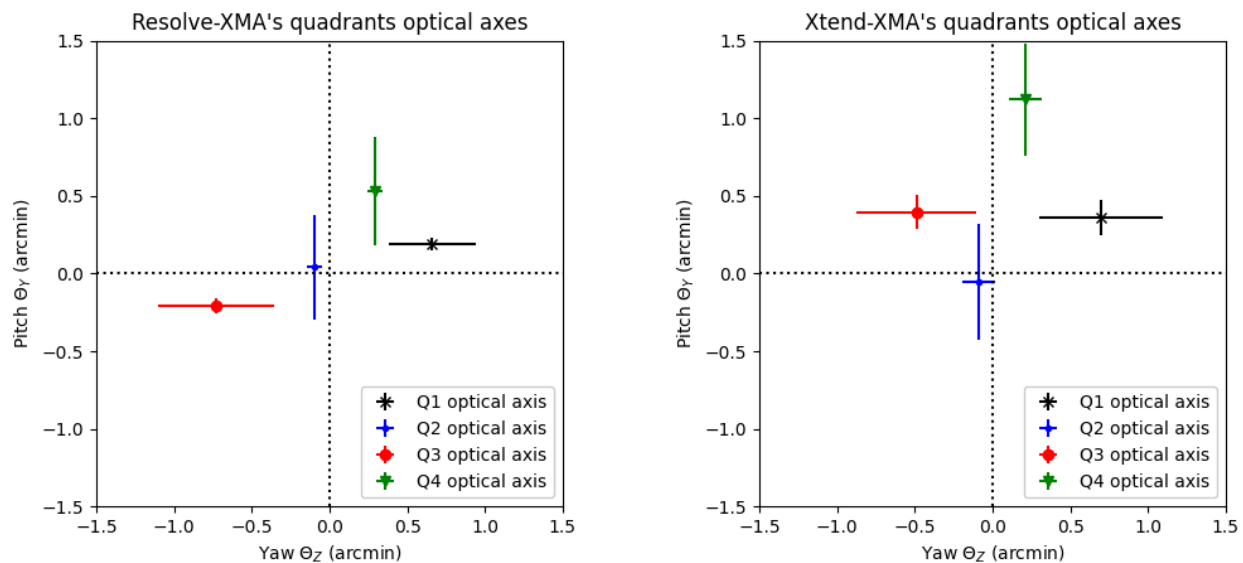


Figure 5. Distribution of the optical axes for the quadrants of Resolve-XMA (left) and Xtend-XMA (right). The measurements of the effective area used to determine these axes have been performed at 6.4 keV, and the origins of the plots represent the optical axes of the whole telescopes (determined from the initial vignetting measurements).

4.2 On-axis effective area

After aligning the telescopes to their respective whole-telescope axes, and determining the quadrants' optical axes at 6.4 keV (see Sec. 4.1), we performed the measurements of the effective area of each quadrant for both XMA, at the whole-telescope axis, at eight energies: Al $K\alpha$ (1.5 keV), Ti $K\alpha$ (4.5 keV), Fe $K\alpha$ (6.4 keV), Cu $K\alpha$ (8.0 keV), Pt $L\alpha$ (9.4 keV), Pt $L\beta$ (11.1 keV), Mo $K\alpha$ (17.5 keV), and Ag $K\alpha$ (22.2 keV, for Resolve-XMA only). The effective area of the whole telescope is calculated as the sum of the effective area of each quadrant. The results of these measurements (with 68% statistical errors) are shown in Tab. 1 and Fig. 6, as well as the requirements. With a total effective area of 587 cm² at 1.5 keV and 419 cm² at 6.4 keV, the measurements clearly show that both XMA meet the effective area requirements of >460 cm² at 1.5 keV and >390 cm² at 6.4 keV.

Table 1. Effective area (in cm²) for both XMA (with 68% statistical errors), at different energies E, for the whole telescope and each quadrant, at the whole telescope axis. Requirements at two energies are also shown. *The effective area at 22.2 keV has a big uncertainty due to a large X-ray background.

E (keV)	1.5	4.5	6.4	8.0	9.4	11.1	17.5	22.2
Resolve-XMA								
Total	584.7 ± 0.4	434.7 ± 0.6	416.0 ± 0.6	345.3 ± 0.8	233.4 ± 0.6	163.4 ± 0.4	38.4 ± 0.2	12*
Q1	145.6 ± 0.2	109.2 ± 0.3	103.6 ± 0.3	85.7 ± 0.4	57.8 ± 0.3	39.5 ± 0.2	9.2 ± 0.1	3*
Q2	148.6 ± 0.2	112.4 ± 0.3	105.5 ± 0.3	88.0 ± 0.4	59.1 ± 0.3	40.6 ± 0.2	9.3 ± 0.1	3*
Q3	147.8 ± 0.2	109.5 ± 0.3	105.8 ± 0.3	86.3 ± 0.4	58.4 ± 0.3	41.2 ± 0.2	10.0 ± 0.1	3*
Q4	142.7 ± 0.2	103.7 ± 0.3	101.1 ± 0.3	85.4 ± 0.4	58.2 ± 0.3	42.1 ± 0.2	10.0 ± 0.1	3*
Xtend-XMA								
Total	589.4 ± 0.4	441.5 ± 0.6	422.2 ± 0.6	349.2 ± 0.8	235.5 ± 0.6	164.5 ± 0.4	37.9 ± 0.1	—
Q1	147.3 ± 0.2	109.9 ± 0.3	106.0 ± 0.3	87.8 ± 0.4	58.4 ± 0.3	41.7 ± 0.2	10.0 ± 0.1	—
Q2	148.3 ± 0.2	112.6 ± 0.3	107.6 ± 0.3	89.0 ± 0.4	60.6 ± 0.3	41.7 ± 0.2	9.7 ± 0.1	—
Q3	147.1 ± 0.2	110.0 ± 0.3	105.0 ± 0.3	86.6 ± 0.4	58.2 ± 0.3	40.4 ± 0.2	8.9 ± 0.1	—
Q4	146.7 ± 0.2	109.0 ± 0.3	103.6 ± 0.3	85.8 ± 0.4	58.3 ± 0.3	40.8 ± 0.2	9.4 ± 0.1	—
Requirements								
Total	> 460	—	> 390	—	—	—	—	—

The statistical error (from the Poisson distribution of the photons) on the measured on-axis effective area is < 1% in all energies, for both XMA. The effective area among individual quadrants is found to vary significantly in all energies (from about 2% to 11% at higher energy). There is very little difference between both XMA, the effective area of Xtend-XMA being larger than the one of Resolve-XMA by only ~ 1%.

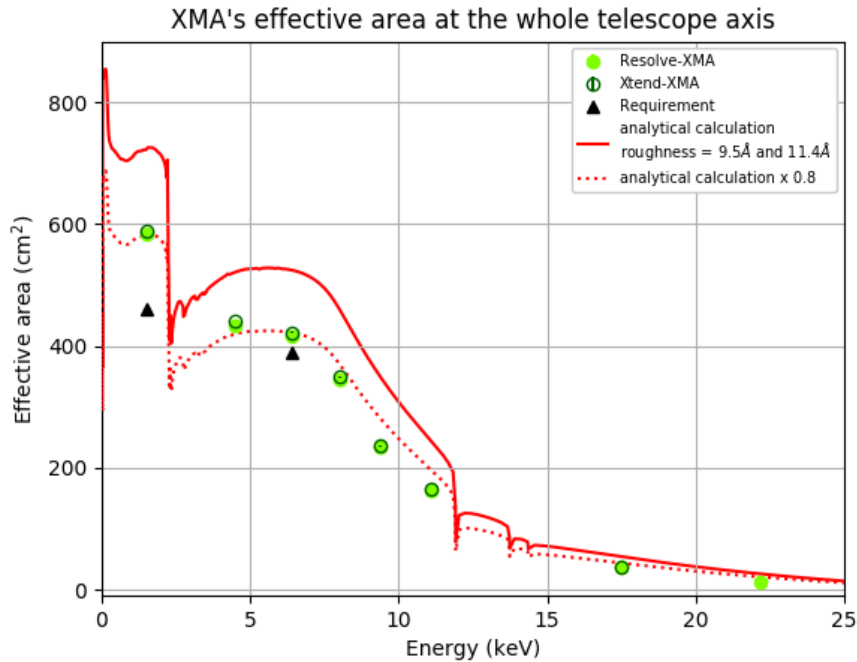


Figure 6. Effective area versus energy, for both XMAs, at the whole-telescope axis (green points). EA requirements are represented by the black triangles. The ideal EA calculated from the design parameters is shown by the solid red line, while 80% of this ideal case is shown by the dashed red curve.

Fig. 6 shows that the measured effective area is about 80% of the ideal value calculated from the design parameters, using the Nevot-Croce model for the reflectivity calculation, the optical constants of the HENKE table,²⁶ and considering that some foils have a roughness of 9.5 Å and some other foils have a roughness of 11.4 Å (red lines).²⁷ This expected departure from ideal values can be explained by a combination of effects: misplacement of the reflectors, misalignments of different parts of the telescope, non-perfect shape of the reflectors (inducing reflection of X-rays on the back of inner reflectors), and reduction of the reflectivity because of the surface roughness of the foils.^{12,21,28} As stated in Sec. 3, the calibration of the telescopes will allow us to make files to be used by a raytracing code to reproduce our ground measurements.

4.3 Off-axis effective area

As explained in the ground calibration plan in Sec. 3, we measured the off-axis responses after getting the on-axis measurements, in seven energies. As the Resolve detector has a small field of view (FoV) of 3' x 3', we measured the angular responses of Resolve-XMA in a small range of off-axis angles, for 4 to 7 off-axis values between 0.5' and 9', and at 2, 4 or 8 roll angles, depending on the energy. The resulting vignetting curves at different energies and roll angles are shown in Fig. 7, and are well fitted with Lorentzian models. The measured off-axis effective area of Resolve-XMA has a statistical error of < 2% in all energies.

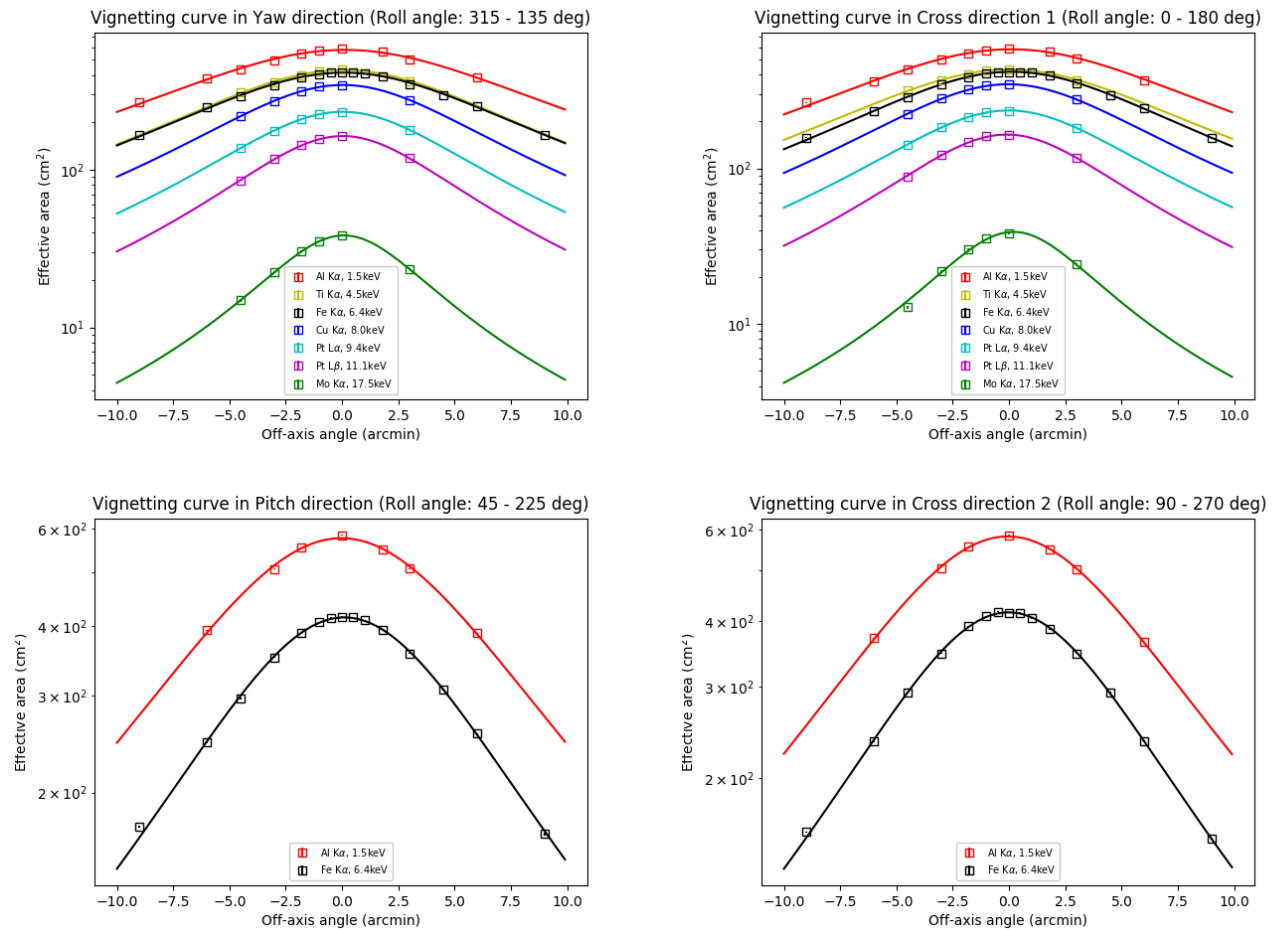


Figure 7. Vignetting curves of all energies, for Resolve-XMA, for all directions, fitted with Lorentzian models.

As the Xtend detector has instead a wide FoV of $38' \times 38'$, we measured the angular responses of Xtend-XMA up to $20'$, for 4 or 5 off-axis values, and at 2 or 8 roll angles, depending on the energy. The resulting vignetting curves at different energies and roll angles are shown in Fig. 8, and are well fitted with the sum of a Lorentzian and a Gaussian model. The measured off-axis effective area of Xtend-XMA has a statistical error of $< 0.3\%$ at 6.4 keV.

The residuals of the off-axis EA measurements to the best-fit models is less than 5%, for both XMAs, as shown for example in the yaw direction, in Fig. 9. This shows that the vignetting curves are well reproduced by the non-phenomenological models we used. However, additional modeling using raytracing simulations is needed to quantify the precision of the relative EA measurements.

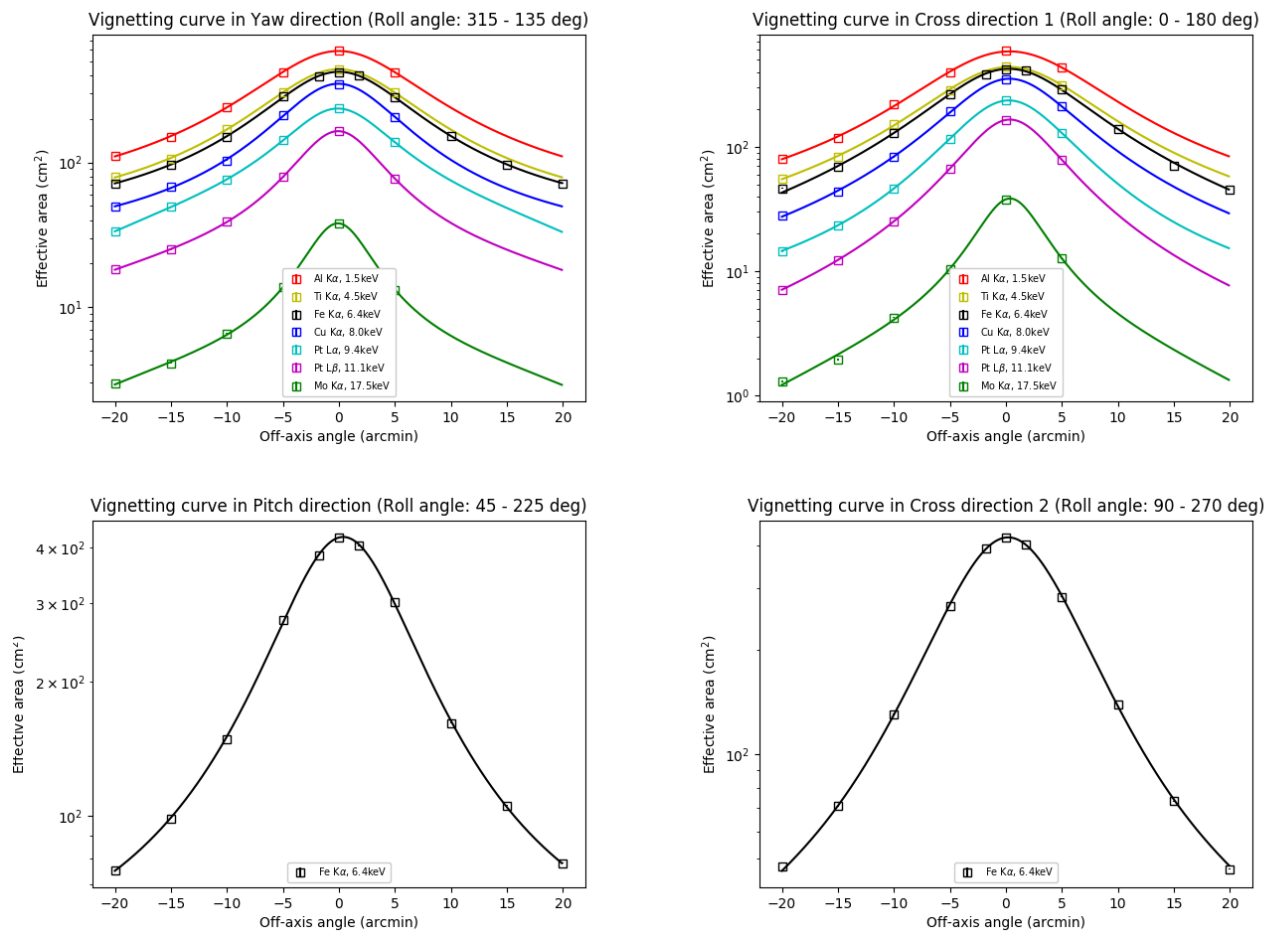


Figure 8. Vignetting curves of all energies, for Xtend-XMA, for all directions, fitted with the sum of Lorentzian and Gaussian models.

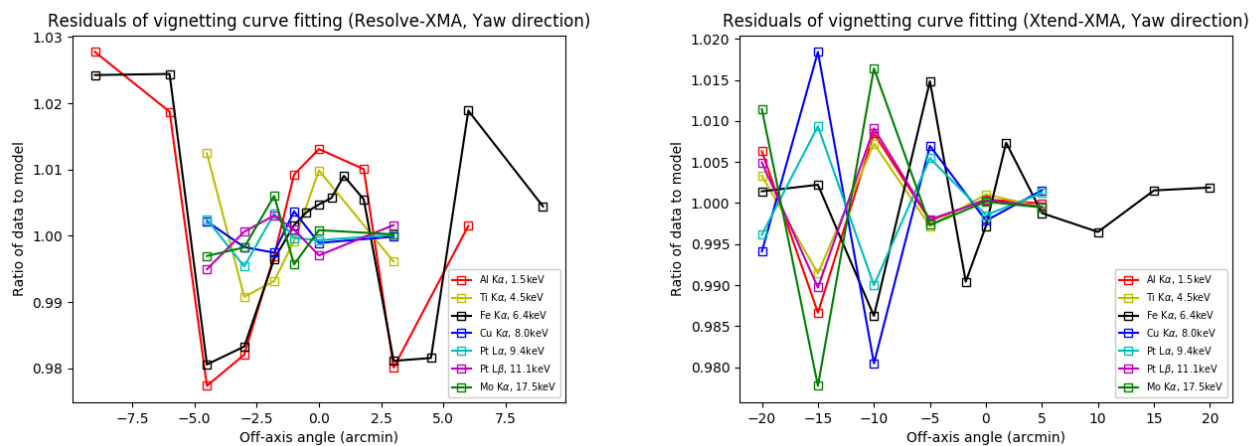


Figure 9. The residuals of the off-axis EA measurements to the best-fit models, at all energies, in the yaw direction, for Resolve-XMA (left) and Xtend-XMA (right).

The fit of vignetting curves at different energies with Lorentzian and possibly Gaussian models allows determining the FoV of each telescope, which corresponds to the Full-Width at Half-Maximum (FWHM) value of the best-fit model. Fig. 10 shows that the FoV decreases with the energy. We note that the mirror FoV is again very similar in both XMA, at all energies.

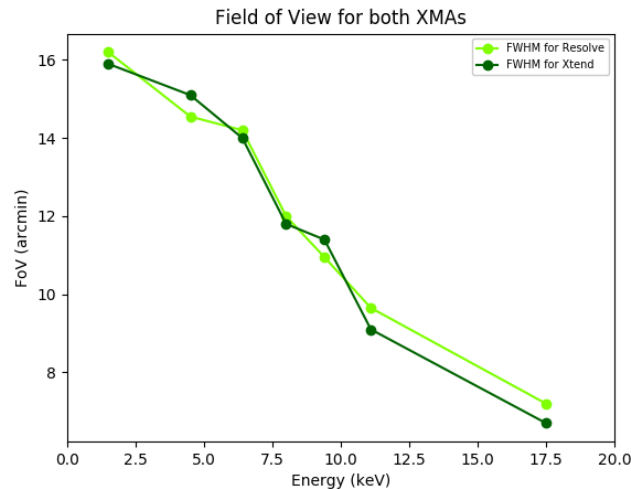


Figure 10. XMA's Field of View, as a function of the energy. The FoV corresponds to the FWHM value determined by fitting the vignetting curves with a Lorentzian and possibly a Gaussian model.

We show below in more details the results of the measurements performed at the particular energy of 6.4 keV. We performed these measurements at the off-axis angles 0.5', 1', 1.8', 3', 4.5', 6' and 9' for Resolve-XMA, and 1.8', 5', 10', 15' and 20' for Xtend-XMA, in 8 roll angles (as shown in Fig. 4 for example). The corresponding vignetting curves for both XMA are shown in Fig. 11. These vignetting curves at 6.4 keV are well fitted with a single Lorentzian model (in the case of Resolve-XMA) or with the sum of a Gaussian and a Lorentzian model (for Xtend-XMA), revealing a very similar mirror FoV of about 14 arcmin for both XMA.

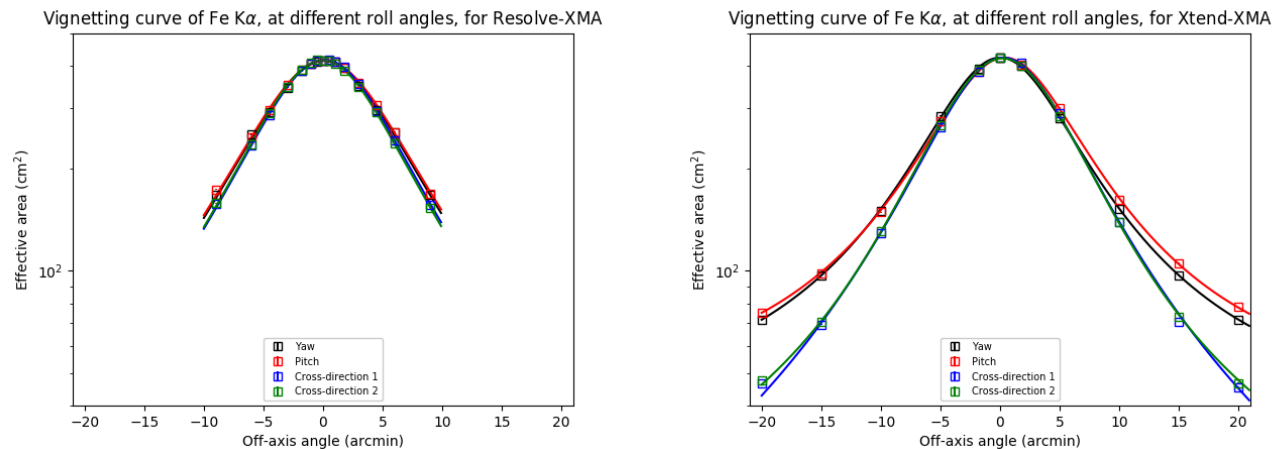


Figure 11. Vignetting curves at 6.4 keV, for Resolve-XMA (left) and Xtend-XMA (right), for 8 roll angles. Yaw direction corresponds to roll angles 315°-135°; Pitch corresponds to 45°-225°; Cross-direction 1 corresponds to 0°-180°; Cross-direction 2 corresponds to 270°-90°. The vignetting curves of Resolve-XMA are well fitted by a single Lorentzian model, while those of Xtend-XMA are better fitted by the sum of a Lorentzian and a Gaussian model.

5. SUMMARY

In this first paper of a series of several publications, we showed part of the results of the ground calibration of the XRISM X-ray Mirror Assemblies at NASA's Goddard beamline. We first presented the measurement setup of the 100 m X-ray beamline facility, as well as the measurement methods we used. We briefly presented the calibration timeline, before reporting on the alignment of the telescopes and the optical axis distribution of the quadrants. We then presented the on-axis and off-axis measurements and the corresponding effective area results for both XMA's. Imaging quality, stray light measurements, and performance verification across the aperture will be presented in separate publications.

ACKNOWLEDGMENTS

XRISM is being developed under an international collaboration of the Japan Aerospace Exploration Agency (JAXA), the National Aeronautics and Space Administration (NASA), and the European Space Agency (ESA). We thank warmly Dr. Yang Soong for his amazing work in the development and manufacturing of the XMA's, and for his support at the beamline facility. We acknowledge the efforts of the instrument teams of XRISM and Hitomi. This study was made possible by the collaborative efforts of members of the Resolve team, which we greatly appreciate. This material is based upon work supported by NASA under the project number FU662038. Part of this work was performed under the auspices of the U.S. Department of Energy by Lawrence Livermore National Laboratory under Contract DE-AC52-07NA27344.

REFERENCES

- [1] XRISM Science Team, "XRISM Quick Reference," *arXiv e-prints*, arXiv:2202.05399 (Feb. 2022).
- [2] Tashiro, M. et al., "Status of x-ray imaging and spectroscopy mission (XRISM)," in [*Society of Photo-Optical Instrumentation Engineers (SPIE) Conference Series*], *Society of Photo-Optical Instrumentation Engineers (SPIE) Conference Series* **11444**, 1144422 (Dec. 2020).
- [3] Terada, Y. et al., "Detailed design of the science operations for the XRISM mission," *Journal of Astronomical Telescopes, Instruments, and Systems* **7**, 037001 (July 2021).
- [4] Tashiro, M. et al., "Concept of the X-ray Astronomy Recovery Mission," in [*Space Telescopes and Instrumentation 2018: Ultraviolet to Gamma Ray*], den Herder, J.-W. A., Nikzad, S., and Nakazawa, K., eds., **10699**, 520 – 531, International Society for Optics and Photonics, SPIE (2018).
- [5] Okajima, T. et al., "Development of the XRISM X-ray Mirror Assembly," in [*American Astronomical Society Meeting Abstracts #235*], *American Astronomical Society Meeting Abstracts* **235**, 373.06 (Jan. 2020).
- [6] Takahashi, T. et al., "Hitomi (ASTRO-H) X-ray Astronomy Satellite," *Journal of Astronomical Telescopes, Instruments, and Systems* **4**, 021402 (Apr. 2018).
- [7] XRISM Science Team, "Science with the X-ray Imaging and Spectroscopy Mission (XRISM)," *arXiv e-prints*, arXiv:2003.04962 (Mar. 2020).
- [8] Soong, Y. et al., "ASTRO-H Soft X-ray Telescope (SXT)," in [*Space Telescopes and Instrumentation 2014: Ultraviolet to Gamma Ray*], Takahashi, T., den Herder, J.-W. A., and Bautz, M., eds., *Society of Photo-Optical Instrumentation Engineers (SPIE) Conference Series* **9144**, 914428 (July 2014).
- [9] Okajima, T. et al., "First measurement of the ASTRO-H soft x-ray telescope performance," in [*Space Telescopes and Instrumentation 2012: Ultraviolet to Gamma Ray*], Takahashi, T., Murray, S. S., and den Herder, J.-W. A., eds., *Society of Photo-Optical Instrumentation Engineers (SPIE) Conference Series* **8443**, 844320 (Sept. 2012).
- [10] Sato, T. et al., "Revealing a detailed performance of the soft x-ray telescopes of the ASTRO-H mission," in [*Space Telescopes and Instrumentation 2014: Ultraviolet to Gamma Ray*], Takahashi, T., den Herder, J.-W. A., and Bautz, M., eds., *Society of Photo-Optical Instrumentation Engineers (SPIE) Conference Series* **9144**, 914459 (July 2014).
- [11] Okajima, T. et al., "First peek of ASTRO-H Soft X-ray Telescope (SXT) in-orbit performance," in [*Space Telescopes and Instrumentation 2016: Ultraviolet to Gamma Ray*], den Herder, J.-W. A., Takahashi, T., and Bautz, M., eds., *Society of Photo-Optical Instrumentation Engineers (SPIE) Conference Series* **9905**, 99050Z (July 2016).

- [12] Iizuka, R. et al., “Ground-based x-ray calibration of the Astro-H/Hitomi soft x-ray telescopes,” *Journal of Astronomical Telescopes, Instruments, and Systems* **4**, 011213 (Jan. 2018).
- [13] Mori, H. et al., “The pre-collimator for the ASTRO-H x-ray telescopes: shielding from stray lights,” in [*Space Telescopes and Instrumentation 2012: Ultraviolet to Gamma Ray*], Takahashi, T., Murray, S. S., and den Herder, J.-W. A., eds., *Society of Photo-Optical Instrumentation Engineers (SPIE) Conference Series* **8443**, 84435B (Sept. 2012).
- [14] Tawara, Y. et al., “Development of ultra-thin thermal shield for ASTRO-H x-ray telescopes,” in [*Society of Photo-Optical Instrumentation Engineers (SPIE) Conference Series*], O’Dell, S. L. and Pareschi, G., eds., *Society of Photo-Optical Instrumentation Engineers (SPIE) Conference Series* **8147**, 814704 (Sept. 2011).
- [15] Tamura, K. et al., “Ground calibration of the X-ray Mirror Assembly for the X-Ray Imaging and Spectroscopy Mission (XRISM) II - Imaging performance and stray light,” in [*Space Telescopes and Instrumentation 2022: Ultraviolet to Gamma Ray*], *Society of Photo-Optical Instrumentation Engineers (SPIE) Conference Series* **12181**, 69 (July 2022).
- [16] Hayashi, T. et al., “Ground calibration of the X-ray Mirror Assembly for the X-Ray Imaging and Spectroscopy Mission (XRISM) III - Performance variation across the aperture,” in [*Space Telescopes and Instrumentation 2022: Ultraviolet to Gamma Ray*], *Society of Photo-Optical Instrumentation Engineers (SPIE) Conference Series* **12181**, 263 (July 2022).
- [17] Suzuki, H. et al., “Development of a powerful x-ray generator with a small spot-size option at ISAS x-ray beamline facility,” in [*Society of Photo-Optical Instrumentation Engineers (SPIE) Conference Series*], *Society of Photo-Optical Instrumentation Engineers (SPIE) Conference Series* **11444**, 114447G (Dec. 2020).
- [18] Gondoin, P. et al., “Calibration of the first XXM flight mirror module: II. Effective area,” in [*X-Ray Optics, Instruments, and Missions*], Hoover, R. B. and Walker, A. B., eds., *Society of Photo-Optical Instrumentation Engineers (SPIE) Conference Series* **3444**, 290–301 (Nov. 1998).
- [19] Kunieda, H. et al., “Thirty-Meter X-Ray Pencil Beam Line at the Institute of Space and Astronautical Science,” *Japanese Journal of Applied Physics* **32**, 4805 (Oct. 1993).
- [20] Tsusaka, Y. et al., “Characterization of the Advanced Satellite for Cosmology and Astrophysics x-ray telescope: preflight calibration and ray tracing,” **34**, 4848–4856 (Aug. 1995).
- [21] Shibata, R. et al., “X-Ray Telescope Onboard Astro-E. II. Ground-Based X-Ray Characterization,” **40**, 3762–3683 (Aug. 2001).
- [22] Hayashi, T. et al., “Upgrade of the 30-m x-ray pencil beam line at the Institute of Space and Astronautical Science,” *Journal of Astronomical Telescopes, Instruments, and Systems* **1**(4), 1 – 7 (2015).
- [23] Zissa, D. E., “AXAF-1 high-resolution mirror assembly image model and comparison with x-ray ground-test image,” in [*X-Ray Optics, Instruments, and Missions II*], Hoover, R. B. and Walker, A. B., eds., *Society of Photo-Optical Instrumentation Engineers (SPIE) Conference Series* **3766**, 36–50 (Sept. 1999).
- [24] Miller, E. D. et al., “Planning in-flight calibration for XRISM,” in [*Society of Photo-Optical Instrumentation Engineers (SPIE) Conference Series*], *Society of Photo-Optical Instrumentation Engineers (SPIE) Conference Series* **11444**, 1144426 (Dec. 2020).
- [25] Loewenstein, M. et al., “The XRISM science data center: optimizing the scientific return from a unique x-ray observatory,” in [*Society of Photo-Optical Instrumentation Engineers (SPIE) Conference Series*], *Society of Photo-Optical Instrumentation Engineers (SPIE) Conference Series* **11444**, 114445D (Dec. 2020).
- [26] Henke, B. L. et al., “X-Ray Interactions: Photoabsorption, Scattering, Transmission, and Reflection at $E = 50\text{--}30,000$ eV, $Z = 1\text{--}92$,” *Atomic Data and Nuclear Data Tables* **54**, 181–342 (July 1993).
- [27] Spiga, D., “Optics for X-ray telescopes: analytical treatment of the off-axis effective area of mirrors in optical modules,” **529**, A18 (May 2011).
- [28] Misaki, K. et al., “X-ray telescope onboard Astro-E. III. Guidelines to performance improvements and optimization of the ray-tracing simulator,” **44**, 916–940 (Feb. 2005).